ISSN (Print) 1226-1750
ISSN (Online) 2233-6656
Journal of Magnetics 28(2), 135-150 (2023) https://doi.org/10.4283/JMAG.2023.28.2.135

The Influence of Shaft Eccentricity on the Magnetic Fluid Sealing Performance

Shicong Li[1], Decai Li[1]*, and Shuangxi Li[2]*

[1]*State Key Laboratory of Tribology, Tsinghua University, Beijing 100084, China*
[2]*College of Mechanical and Electrical Engineering, Beijing University of Chemical Technology, Beijing 100029, China*

(Received 31 January 2023, Received in final form 18 June 2023, Accepted 22 June 2023)

This manuscript delves into the impact of shaft eccentricity and diameter on the pressure resistance and magnetic force of a magnetic fluid seal (MFS), through both magnetic circuit analysis method (MCAM) and finite element method (FEM). The study proposes a systematic approach to enhance the performance of eccentric MFS based on MCAM. The results show a near-linear decrease in the pressure resistance of the MFS with increasing eccentricity, with a maximum decline of 65 %. However, the MFS model with a 100 mm shaft diameter renders more precise results in predicting the sealing performance for larger shaft diameters since the pressure resistance decrease remains below 5 % as shaft diameter is increased. The optimal range of pole tooth structure parameters has also been determined. Remarkably, the proposed method affords a precise analysis of the performance of large-diameter eccentric MFS, which is not feasible using two-dimensional axisymmetric magnetic field models.

Keywords : magnetic fluid seal, shaft eccentricity, sealing performance, magnetic circuit analysis method

1. Introduction

Magnetic fluid seal (MFS) has been widely used in aerospace [1, 2], defense [3, 4], machinery [5, 6], chemical [7], petroleum [8], and instrumentation [9] because of its simple structure, zero leakage, long life and other advantages [10]. MFS with shaft diameter over 150 mm is large diameter seal [11]. Currently, MFS has been widely used in vacuum or gas environments with small diameters and low rotational speeds [12, 13], while MFS with large diameter is the focus of current research. MFS mostly uses rolling bearings to limit the relative position of the shaft and the pole shoe. When the shaft diameter is small, the bearing clearance is 1 order of magnitude lower than the sealing gap, and the influence on the sealing performance can be ignored. However, when the shaft diameter is large, especially when the shaft diameter exceeds 500 mm, the radial internal clearance of C2 deep groove ball bearings can reach 100 μm, which is in the same order of magnitude as the sealing gap. In addition, MFS is inevitably affected by machining and assembly errors, shaft oscillation vibration and other factors during manufacture, installation and use, making the shaft eccentric with respect to the pole shoe. The shaft eccentricity may lead to friction and wear between the shaft and the pole teeth and damage the seal structure [14], and the shaft eccentricity leads to a significant reduction of the magnetic field strength in the sealing gap [15], which is highly susceptible to seal failure.

The sealing gap of large shaft diameter MFS tends to be larger, which can reduce the effect of shaft eccentricity on the sealing performance. The sealing performance can also be improved by changing the form of the magnetic source [16], optimizing the pole tooth structure [17], and selecting a magnetic fluid with high saturation magnetization strength [18]. For MFS with a large sealing gap, the sealing performance of individual pole tooth is significantly reduced [19], and more pole teeth as well as larger axial dimensions are required to achieve a stable sealing performance.

There are more studies on MFS with large diameters and sealing gap, while fewer studies on the influence of shaft eccentricity on the sealing performance of MFS. Zhang *et al*. [20, 21] obtained the relationship between the shaft eccentricity and the sealing performance of MFS by deriving the electromagnetic theory. However, the theoretical derivation assumes that the magnetic field

©The Korean Magnetics Society. All rights reserved.
*Co-corresponding author: Tel: +86 13651206606(Decai Li), +86 13691418726(Shuangxi Li)
Fax: +86 13691418726, e-mail: lidecai@tsinghua.edu.cn(Decai Li), buctlsx@126.com(Shuangxi Li)

© 2023 Journal of Magnetics

distribution does not change along the axial direction, which is not applicable to the MFS with multi-pole teeth. Zhang [22] and Yang *et al.* [23] established a 3-D shaft eccentricity magnetic field model and analyzed the relationship between the pressure resistance of MFS and the shaft eccentricity, but the effect of shaft diameter was not considered. Compared with the MFS structure with sealing gap, the MFS structure aiming to accommodate shaft eccentricity can improve the sealing performance of individual pole teeth and reduce the seal size. Therefore, it is of great significance to analyze the influence of shaft eccentricity on the sealing performance of MFS and propose corresponding improvement measures for the application of the MFS with large diameter.

In this paper, the sealing performance and influencing factors of eccentric MFS are analyzed by magnetic circuit analysis method (MCAM) and finite element method (FEM). In the MCAM, the reluctance of the sealing gap when the shaft is eccentric is derived, and the theoretical calculation method for the sealing performance of the eccentric MFS is obtained. In the FEM, a 3-D eccentric magnetic field model is established, and the magnetic field distribution of the eccentric MFS is obtained by solving Maxwell's equations and compared with the results of the MCAM. The variation of sealing performance of the MFS with shaft diameter is investigated. Based on the MCAM, the method to improve the performance of eccentric MFS is studied, in order to provide guidance for the design and optimization of MFS with large eccentricity.

2. Analytical Model of MFS

2.1. Typical structure of MFS

A typical structure of MFS is shown in Fig. 1, which consists of a non-magnetic shell, permanent magnet, shaft, pole shoe, magnetic fluid and O-ring. The structural parameters of the MFS analyzed in this paper are shown

Table 1. Structural Parameters of MFS.

Parameter	Value
Shaft diameter d (mm)	40-160
Sealing gap L_g (mm)	0.1, 0.2, 0.3
Height of pole tooth L_h (mm)	1
Thickness of pole tooth L_t (mm)	0.5
Width of tooth slot L_s (mm)	1
Number of pole teeth n_p	12
Inner diameter of permanent magnet d_i (mm)	$d+8$
Width of permanent magnet W (mm)	6
Thickness of permanent magnet T_h (mm)	4

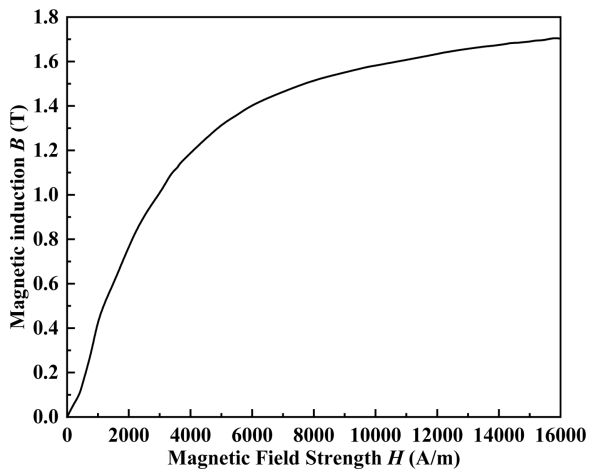

Fig. 2. B-H Curve of 2Cr13.

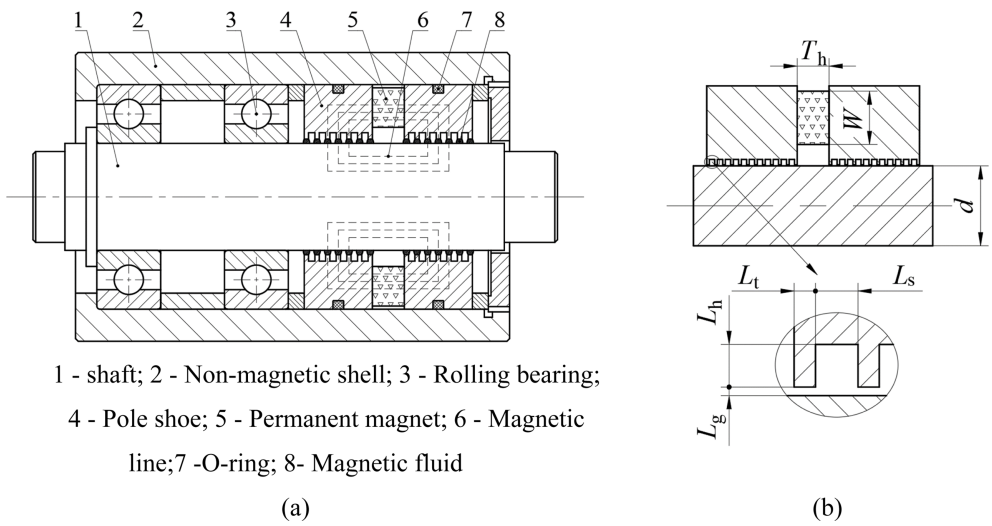

Fig. 1. Typical structure and dimensions of MFS: (a) Schematic Diagram of MFS; (b) Basic dimensions of MFS.

in Table 1. The material of both shaft and pole shoe is 2Cr13. The B-H curve for 2Cr13 is illustrated in Fig. 2. The permanent magnet material grade is N35, and its primary features are a remanent magnetization of 1.18 T, reversible permeability of 1.05, and maximum magnetic energy product of 263 kJ/m^3. The magnetic fluid is an ester-based magnetic fluid with a saturation magnetization strength of 31.04 kA/m.

2.2. Basic assumptions

(1) During normal operation, the MFS is in a state of non-contact, implying that the pole shoe does not touch the shaft, and magnetic fluid is present between each pole tooth and the shaft.

(2) The magnetic fluid is incompressible, and the flow is a constant isothermal flow.

(3) The effects of gravity and centrifugal force on the magnetic fluid and MFS are neglected.

2.3. Mathematical model

2.3.1. Magnetic field analysis

There is no free current in the MFS, and the equation for the magnetic scalar potential (φ_m) in the Cartesian coordinate system is as follows [24]:

$$\frac{\partial}{\partial x}\left(\mu_0\mu_r\frac{\partial\varphi_m}{\partial x}\right)+\frac{\partial}{\partial y}\left(\mu_0\mu_r\frac{\partial\varphi_m}{\partial y}\right)+\frac{\partial}{\partial z}\left(\mu_0\mu_r\frac{\partial\varphi_m}{\partial z}\right)=0 \quad (1)$$

Where μ_0 indicates the vacuum permeability, μ_r indicates the relative permeability of the material, and φ_m indicates the magnetic scalar potential.

The boundary at infinity satisfies:

$$\varphi_m = 0 \quad (2)$$

The magnetic force (F_s) on the shaft can be calculated using the Maxwell stress tensor [25] as:

$$\vec{F}_s = -\oint_S \boldsymbol{n}\boldsymbol{T}ds \quad (3)$$

Where S indicates the integral surface of the shaft, $\boldsymbol{n}$ indicates the normal vector of the integral surface of the shaft, and $\boldsymbol{T}$ indicates the Maxwell stress tensor of the integral surface of the shaft, which can be expressed as:

$$\boldsymbol{T} = -\frac{1}{2}\boldsymbol{H}\cdot\boldsymbol{B}+\boldsymbol{H}\boldsymbol{B}^{\mathrm{T}} \quad (4)$$

Where $\boldsymbol{H}$ indicates the magnetic field strength, $\boldsymbol{B}$ indicates the magnetic induction, and $\boldsymbol{B} = \mu_0\boldsymbol{H}$.

2.3.2. Magnetic field calculation

A comprehensive 3D magnetic field model was established in COMSOL for the MFS. When eccentric, the shaft can be viewed as symmetrical, enabling the creation of a 1/2 model, as demonstrated in Fig. 3(a). In order to ensure both high precision and small computational scale, a hexahedral mesh was employed for the shaft, pole shoe, permanent magnet, and sealing gap. Meanwhile, a tetrahedral mesh was implemented for the air domain, as depicted in Fig. 3(b). The magnetic lines in the air domain are circular curves that traverse through the permanent magnet cross section and remain parallel to the outer boundary and the symmetry plane of the model. These particular magnetic lines were defined as $\boldsymbol{n}\cdot\boldsymbol{B} = 0$, delimiting the magnetic insulation boundary in COMSOL.

2.3.3. Sealing performance of MFS

The magnetic fluid in the sealing gap of the MFS is subject to various influences, including magnetic field force, surface pressure, and fluid motion. The internal

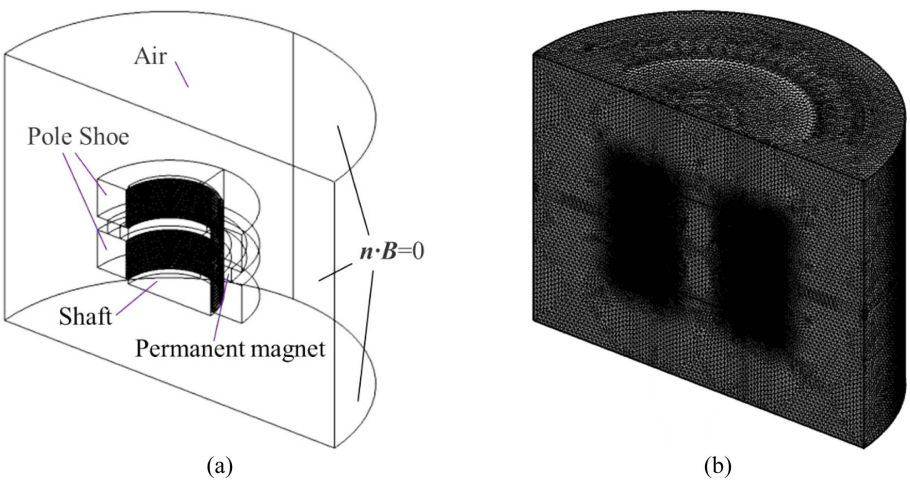

Fig. 3. Magnetic field model and mesh of eccentric MFS: (a) Computational model; (b) Mesh.

pressure of the magnetic fluid can be derived utilizing Bernoulli's equation [26], shown as follows:

$$p+\frac{1}{2}\rho_{\mathrm{m}}V^{2}+\rho_{\mathrm{m}}gh_{\mathrm{m}}-\mu_{0}\int_{0}^{H}MdH=C \tag{5}$$

Where p indicates the pressure of the magnetic fluid, ρ_{m} indicates the density of the magnetic fluid, V indicates the velocity of the magnetic fluid, h indicates the distance between the magnetic fluid and the reference point, g indicates the gravitational acceleration, M indicates the magnetization strength of the magnetic fluid, and C indicates a constant.

Most of the magnetic fluid in the pole tooth region becomes magnetically saturated, and neglecting the impact of gravity, the pressure resistance of the MFS can be calculated as:

$$\Delta p=\mu_{0}\int_{H_{\min}}^{H_{\max}}MdH=\mu_{0}M_{\mathrm{s}}\left(H_{\max}-H_{\min}\right)=M_{\mathrm{s}}\left(B_{\max}-B_{\min}\right) \tag{6}$$

Where $H_{\max}$ and $H_{\min}$ indicate the maximum and minimum magnetic field strengths in the sealing gap, respectively, while $B_{\max}$ and $B_{\min}$ indicate the maximum and minimum magnetic inductions in the same region. M_{s} indicates the saturation magnetization strength of the magnetic fluid.

The pressure resistance of the MFS with multi-pole teeth can be expressed as:

$$\Delta p=M_{\mathrm{s}}\sum_{i=1}^{n_{\mathrm{p}}}\left(B_{\max}^{i}-B_{\min}^{i}\right) \tag{7}$$

where $B_{\max}^{i}$ and $B_{\min}^{i}$ indicate the maximum and minimum magnetic inductions within the magnetic fluid at the ith pole tooth, respectively.

Typically, $B_{\max}$ and $B_{\min}$ are dependent on the selected position. As per the analysis of the magnetic field of the MFS in literature [27], the middle position of the sealing gap is selected to calculate $B_{\max}$ and $B_{\min}$. As shown in Fig. 4, point M represents the middle position of the side with smaller sealing gap, while point N represents the middle position of the side with larger sealing gap. The

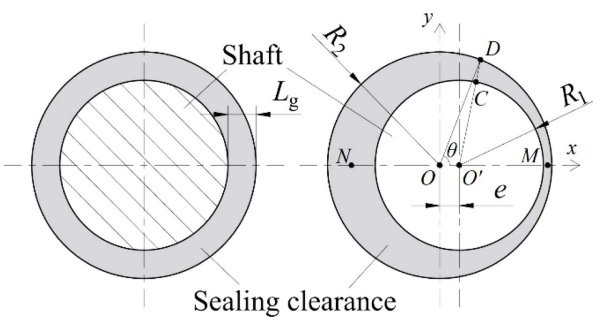

Fig. 4. Diagram of sealing gap of eccentric MFS.

position of point M and point N depends on the eccentricity and the sealing gap. A straight line, parallel to the axis, is drawn at points M and N, respectively, and $B_{\max}$ at each pole tooth position and $B_{\min}$ at each tooth slot position are computed and substituted into Eq. (7) to calculate the pressure resistance.

The sealing gap (L_{g}) is defined as the distance between the inner surface of the pole tooth and the outer surface of the shaft on one side, the value of shaft eccentricity (e) is defined as the distance between the axis of the shaft and the axis of the inner surface of the pole tooth, and the eccentricity (ε) is defined as the ratio of e to L_{g}.

2.4. Magnetic circuit analysis method

In the magnetic field, B is the ratio of magnetic flux (Φ) to the flux area (A), expressed as $B = \Phi/A$. Φ is the ratio of magnetic motive force (F_{m}) to reluctance (R), expressed as $\Phi = F_{\mathrm{m}}/R$. The measure of ease with which flux is established in a medium is permeance (λ), defined as the reciprocal of reluctance, expressed as $\lambda = 1/R$. Therefore, B is inversely proportional to R and positively proportional to λ, expressed as $B \propto 1/R$, or $B \propto \lambda$. The trend of B in the sealing gap at eccentricity can be derived by obtaining the trend of R or λ in the magnetic circuit of the MFS.

Figure 5(a) displays the equivalent magnetic circuit of the MFS with multi-pole teeth illustrated in Fig. 1. The permanent magnet is modeled as a constant magnetic motive force source (F_{c}) aligned in series with a constant internal reluctance (R_{m}). The magnetic motive force transmitted to the outer magnetic circuit is determined by the reluctance of the outer circuit. Similarly, all components and sealing gaps in the outer magnetic circuit are regarded as the equivalent reluctances.

It is important to note that theoretically, the reluctances of the pole shoe (R_{p}) and shaft (R_{a}) should be split into several parts according to the thickness of the pole tooth (L_{t}) and tooth slot (L_{s}), and then connected in series with the reluctances of the pole tooth (R_{t}) and pole tooth sealing gap (R_{gt}), as well as the reluctance of tooth slot sealing gap (R_{gs}), as shown in Fig. 5(b). However, this approach would significantly exacerbate the complexity of the total magnetic resistance calculation. Furthermore, each fraction of the R_{p} and R_{a} is approximately one thousandth of the R_{gt} and R_{gs}. Thus, for simplicity, their impact on the magnetic circuit is ignored, and they are analyzed as a whole, resulting in the equivalent magnetic circuit illustrated in Fig. 5(a).

As depicted in Fig. 4, the sealing gap between the pole tooth and shaft is defined by the circle with radius R_2, being the inner surface of the pole tooth with center O,

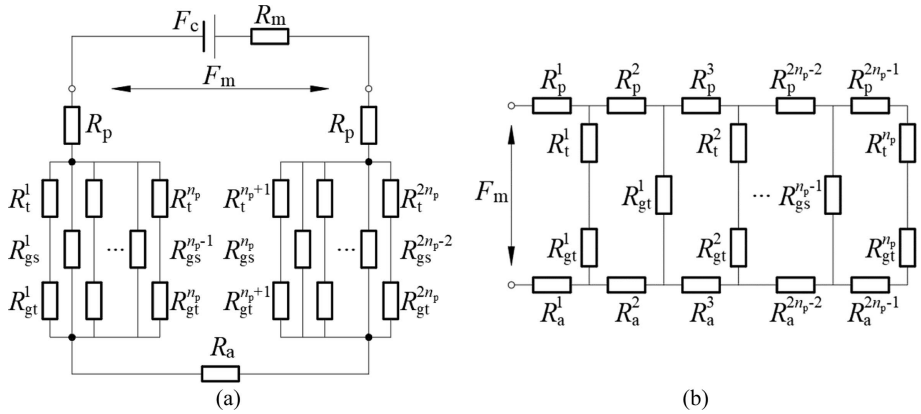

Fig. 5. Equivalent magnetic circuit of the MFS with multi-pole teeth: (a) simplified equivalent magnetic circuit; (b) actual equivalent magnetic circuit.

and the circle with radius R_1, corresponding to the outer surface of the shaft with center O'. Herein, $R_1 = d/2$ and $R_2 = R_1 + L_g$. In case of zero eccentricity ($e = 0$), the permeability of the pole tooth sealing gap (λ_{gt}) can be calculated by according to Eq. (8).

$$\lambda_{gt} = \frac{2\mu_0 \pi R_1 L_t}{L_g} \tag{8}$$

The permeability of the tooth slot sealing gap (λ_{gs}) is calculated according to Eq. (9) based on the substitution angle method.

$$\lambda_{gs} = 2\int_0^{\frac{L_s}{2}} \frac{2\mu_0 \pi R_1}{L_g + \beta x} \mathrm{d}x = \frac{4\mu_0 \pi R_1}{\beta} \ln\left(1 + \frac{\beta L_s}{2L_g}\right) \tag{9}$$

Where β is taken as 1~1.1.

When the seal is eccentric, the distance between the outer surface of the shaft and the inner surface of the pole tooth is not a constant value. As a result, the theoretical permeability of the sealing gap must be calculated using the calculus integration method. According to electromagnetism, electromagnetic waves propagate along the shortest path in the medium, or in other words, the magnetic flux always flows along the path of least resistance. Therefore, when the shaft is eccentric, L_g in Eqs. (8) and (9) should be represent the shortest distance from any micro-element on the inner surface of the pole tooth to the outer surface of the shaft. In Fig. 4, let θ be the angle between any point D on the inner surface of the pole tooth and the x-axis, and let point C be the intersection of DO' and circle O'. Then, CD is the shortest distance from point D to circle O'. The length of CD can be obtained using the cosine theorem as shown in Eq. (10).

$$|CD| = |O'D| - |O'C| = \sqrt{R_2^2 + e^2 - 2R_2 e\cos\theta} - R_1 \tag{10}$$

The permeability of the pole tooth sealing gap (λe gt) and tooth slot sealing gap (λe gs) at eccentricity are given by Eq. (11) and Eq. (12), respectively.

$$\lambda_{gt}^{e} = \int_0^{2\pi} \frac{\mu_0 R_1 L_t \mathrm{d}\theta}{|CD|} \tag{11}$$

$$\lambda_{gs}^{e} = 2\int_0^{2\pi}\int_0^{\frac{L_s}{2}} \frac{\mu_0 R_1}{|CD| + \beta x} \mathrm{d}x\mathrm{d}\theta = \int_0^{2\pi} \frac{2\mu_0 R_1}{\beta} \ln\left(1 + \frac{\beta L_s}{2|CD|}\right) \mathrm{d}\theta \tag{12}$$

R_m, R_t, R_p and R_a are calculated according to Eq. (13) through (16), respectively.

$$R_m = \frac{T_h}{\mu_0 \mu_{r1} A_m} \tag{13}$$

$$R_t = \frac{L_h}{2\mu_0 \mu_{r2} \pi R_2 L_t} \tag{14}$$

$$R_p = \frac{n_p L_t + (n_p - 1) L_s}{\mu_0 \mu_{r2} A_p} \tag{15}$$

$$R_a = \frac{2n_p L_t + 2(n_p - 1) L_s + T_h}{\mu_0 \mu_{r2} \pi R_1^2} \tag{16}$$

Where μ_{r1} and μ_{r2} indicate the relative permeability of the permanent magnet and the permeable material, respectively. A_m and A_p indicate the perpendicular cross-sectional area of the permanent magnet and pole shoe with respect to the direction of magnetic flux.

If the circumferential magnetic flux in the permanent magnet, pole shoe, sealing gap and shaft can be neglected and only the axial and radial magnetic flux is considered, then each reluctance in the magnetic circuit can be regarded as formed by an infinite number of reluctance microelements in parallel. For instance, with respect to

R_p, the cross section of the pole shoe within the range of $d\theta$ is an annular sector with a circular center angle $d\theta$, and its reluctance can be expressed as follows:

$$R_p^d = \frac{n_p L_t + (n_p - 1) L_s}{\mu_0 \mu_{r2} A_p \frac{d\theta}{2\pi}} \tag{17}$$

The number of annular sector is $2\pi/d\theta$, and their reluctance when connected in parallel is:

$$R_p' = \frac{1}{\frac{2\pi}{d\theta} \cdot \frac{1}{R_p^d}} = \frac{1}{\frac{2\pi}{d\theta} \cdot \frac{\mu_0 \mu_{r2} A_p \frac{d\theta}{2\pi}}{n_p L_t + (n_p - 1) L_s}} = \frac{n_p L_t + (n_p - 1) L_s}{\mu_0 \mu_{r2} A_p \frac{d\theta}{2\pi}} = R_p \tag{18}$$

The aforementioned equation illustrates that computing the reluctance of each micro-element initially and then paralleling their reluctances to obtain the total reluctance is the same as directly calculating the total reluctance. Consequently, the magnetic field of the eccentric MFS can be calculated by this method.

Eqs. (11) and (12) can be expressed as follows, using the definite integral formula:

$$\lambda_{gt}^e = \int_0^{2\pi} \frac{\mu_0 R_1 L_t d\theta}{|CD|} = \lim_{m \to +\infty} \sum_{i=1}^{m} \frac{\mu_0 R_1 L_t}{|CD|} \frac{2\pi}{m} \tag{19}$$

$$\lambda_{gs}^e = \int_0^{2\pi} \frac{2\mu_0 R_1}{\beta} \ln\left(1 + \frac{\beta L_s}{2|CD|}\right) d\theta = \lim_{m \to +\infty} \sum_{i=1}^{m} \frac{2\mu_0 R_1}{\beta} \ln\left(1 + \frac{\beta L_s}{2|CD|}\right) \frac{2\pi}{m} \tag{20}$$

Where $m = 2\pi/d\theta$.

Therefore, in the range of $d\theta$, the permeability of the pole tooth sealing gap (λ_{gt}^{ed}) and the permeability of the tooth slot sealing gap (λ_{gs}^{ed}) are as follows:

$$\lambda_{gt}^{ed} = \frac{\mu_0 R_1 L_t}{|CD|} d\theta \tag{21}$$

$$\lambda_{gs}^{ed} = \frac{2\mu_0 R_1}{\beta} \ln\left(1 + \frac{\beta L_s}{2|CD|}\right) d\theta \tag{22}$$

In the range of $d\theta$, the reluctance of the pole tooth sealing gap (R_{gt}^{ed} and the reluctance of the tooth slot sealing gap (R_{gs}^{ed}) are as follows:

$$R_{gt}^{ed} = \frac{1}{\lambda_{gt}^{ed}} = \frac{|CD|}{\mu_0 R_1 L_t d\theta} \tag{23}$$

$$R_{gs}^{ed} = \frac{1}{\lambda_{gs}^{ed}} = \frac{\beta}{2\mu_0 R_1 \ln\left(1 + \frac{\beta L_s}{2|CD|}\right) d\theta} \tag{24}$$

In the range of $d\theta$, the reluctance of permanent magnet (R_m^d), reluctance of pole tooth (R_t^d, reluctance of pole shoe (R_p^d), and reluctance of shaft (R_a^d) are as follows:

$$R_m^d = \frac{T_h}{\mu_0 \mu_{r1} A_m \frac{d\theta}{2\pi}} \tag{25}$$

$$R_t^d = \frac{L_h}{\mu_0 \mu_{r2} R_2 L_t d\theta} \tag{26}$$

$$R_p^d = \frac{n_p L_t + (n_p - 1) L_s}{\mu_0 \mu_{r2} A_p \frac{d\theta}{2\pi}} \tag{27}$$

$$R_a^d = \frac{2 n_p L_t + 2(n_p - 1) L_s + T_h}{\mu_0 \mu_{r2} R_1^2 \frac{d\theta}{2}} \tag{28}$$

In the range of $d\theta$, the total reluctance of the polar tooth sealing gap (R_{t+gt}^d) and the total permeability of the polar tooth sealing gap (λ_{t+gt}^d) formed by the series connection of R_t^d and R_{gt}^{ed} are as follows:

$$R_{t+gt}^d = R_t^d + R_{gt}^{ed} \tag{29}$$

$$\lambda_{t+gt}^d = \frac{1}{R_{t+gt}^d} \tag{30}$$

In the range of $d\theta$, the total reluctance of sealing gap (R_{pa}^d) and total permeability of sealing gap (λ_{pa}^d) formed by the parallel connection of R_{t+gt}^d and R_{gs}^{ed} are as follows:

$$R_{pa}^d = \frac{1}{n_p \frac{1}{R_{t+gt}^d} + (n_p - 1) \frac{1}{R_{gs}^{ed}}} = \frac{1}{n_p \lambda_{t+gt}^d + (n_p - 1) \lambda_{gs}^{ed}} \tag{31}$$

$$\lambda_{pa}^d = \frac{1}{R_{pa}^d} = n_p \lambda_{t+gt}^d + (n_p - 1) \lambda_{gs}^{ed} \tag{32}$$

In the range of $d\theta$, the total reluctance of the MFS (R_{total}^d) and total permeability of the MFS (λ_{total}^d) are as follows:

$$R_{total}^d = R_m^d + 2R_p^d + 2R_{pa}^d + R_a^d \tag{33}$$

$$\lambda_{total}^d = \frac{1}{R_{total}^d} \tag{34}$$

In order to obtain the magnetic induction of the sealing gap, the magnetic motive force of the sealing gap also needs to be calculated. According to electromagnetic theory, the magnetic induction lines in space are closed curves that do not intersect each other. Each magnetic

induction line in the MFS starts from one side of the permanent magnet, passes through the pole shoe, the sealing gap and the shaft, and then returns to the other side of the permanent magnet. The total magnetic motive force of each magnetic induction line is F_c, so the magnetic motive force corresponding to each reluctance can be calculated from the reluctance through which the magnetic induction line passes. The magnetic motive force of the sealing gap can be expressed as:

$$F_p^d = F_c \cdot \frac{R_{pa}^d}{R_{total}^d} \tag{35}$$

Where $F_c = H_c \cdot T_h$, H_c indicates coercive force of the permanent magnet, and T_h indicates the thickness of the permanent magnet.

The magnetic induction of the pole tooth sealing gap (B_{gt}) and the magnetic induction of the tooth slot sealing gap (B_{gs}) can be expressed as follows, respectively:

$$B_{gt} = \frac{\Phi_p^d}{A_{gt}^d} = \frac{F_p^d}{R_{t+gt}^d A_{gt}^d} = \frac{F_p^d}{\left(R_t^d + R_{gt}^{ed}\right) A_{gt}^d} \tag{36}$$

$$B_{gs} = \frac{\Phi_p^d}{A_{gs}^d} = \frac{F_p^d}{R_{gs}^{ed} A_{gs}^d} \tag{37}$$

Where $A_{gt}^d = R_1 L_t \mathrm{d}\theta$ indicate the magnetic flux area of the sealing gap of the pole tooth in the range of $\mathrm{d}\theta$, $A_{gs}^d = R_1 L_s \mathrm{d}\theta$ indicates the magnetic flux area of the sealing gap of the tooth slot in the range of $\mathrm{d}\theta$, and the $\mathrm{d}\theta$ in A_{gt}^d and A_{gs}^d exactly cancels out with $1/\mathrm{d}\theta$ in R_{gt}^{ed} and R_{gs}^{ed}, so B_{gt} and B_{gs} can be calculated by Eqs. (36) and (37) respectively.

According to Eq. (7), the pressure resistance of the MFS can be expressed as:

$$\Delta p = M_s \sum_{i=1}^{n_p} \left(B_{gt}^i - B_{gs}^i\right) = n_p M_s \left(\frac{F_p^d}{R_{t+gt}^d A_{gt}^d} - \frac{F_p^d}{R_{gs}^{ed} A_{gs}^d}\right) \tag{38}$$

3. Analysis of Eccentricity Effect on the Performance of MFS

3.1. Calculation results of MCAM

Figure 6 shows the distribution of λ_{pa}^d. As ε increases, λ_{pa}^d increases at $\theta = 0$ while decreasing at $\theta = \pi$. At $\theta = 0.5\pi$ and $\theta = 1.5\pi$, λ_{pa}^d remains unchanged. The change rate of λ_{pa}^d is larger at $\theta = 0$ compared to $\theta = \pi$. According to Eq. (32), λ_{pa}^d is related to λ_{t+gt}^d and λ_{gs}^{ed}. To further analyze the magnetic field variation, the variation of the λ_{t+gt}^d and λ_{gs}^{ed} with ε are extracted at $\theta = 0$ and $\theta = \pi$, respectively, as shown in Fig. 7.

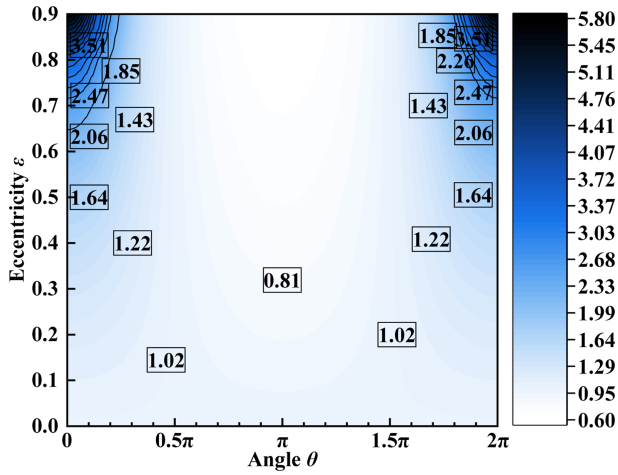

Fig. 6. (Color online) Distribution of λ_{pa}^d in the sealing gap (ratio to λ_{pa}^d at $\theta = 0$ and $\varepsilon = 0$).

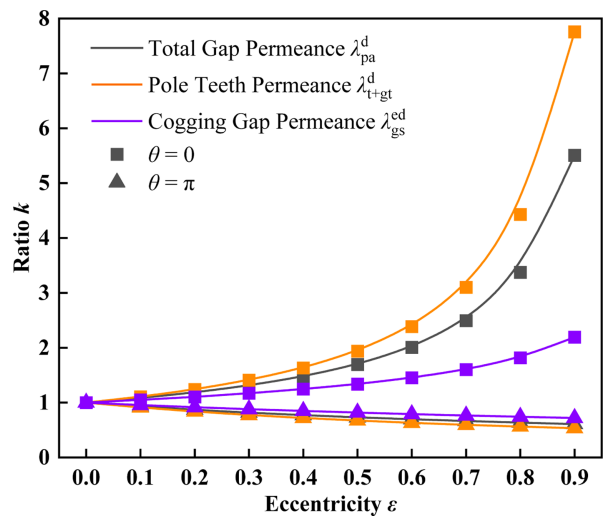

Fig. 7. (Color online) Permeance vs. eccentricity (ratio to λ_{pa}^d, λ_{t+gt}^d and λ_{gs}^{ed} at $\theta = 0$ and $\varepsilon = 0$, respectively).

According to Eq. (30), λ_{t+gt}^d is related to R_t^d and R_{gt}^{ed}. According to Eq. (23), R_{gt}^{ed} is proportional to $|CD|$. When ε increases from 0 to 0.9, at $\theta = 0$, $|CD|$ decreases from L_g to 0.1 times L_g and R_{gt}^{ed} decreases by 90%, while at $\theta = \pi$, $|CD|$ increases from L_g to 1.9 times L_g and R_{gt}^{ed} increases by 0.9 times. The variation of L_g is the same at the same eccentricity, but the variation of R_{gt}^{ed} is very different. In addition, R_t^d is constant and is about 0.03 times of R_{gt}^{ed} at $\theta = 0$ and $\varepsilon = 0$. This causes λ_{t+gt}^d to increase by 6.7 times at $\theta = 0$ and decrease by around 47 % at $\theta = \pi$. When $\varepsilon = 0.9$, at $\theta = 0$, R_t^d is about 0.3 times of R_{gt}^{ed}, and the influence of R_t^d is not negligible; while at $\theta = \pi$, R_t^d is only 0.03 times that of R_{gt}^{ed}, and the influence of R_t^d can be neglected.

According to Eq. (22), λ_{gs}^{ed} is proportional to $\ln[1+\beta L_s/$

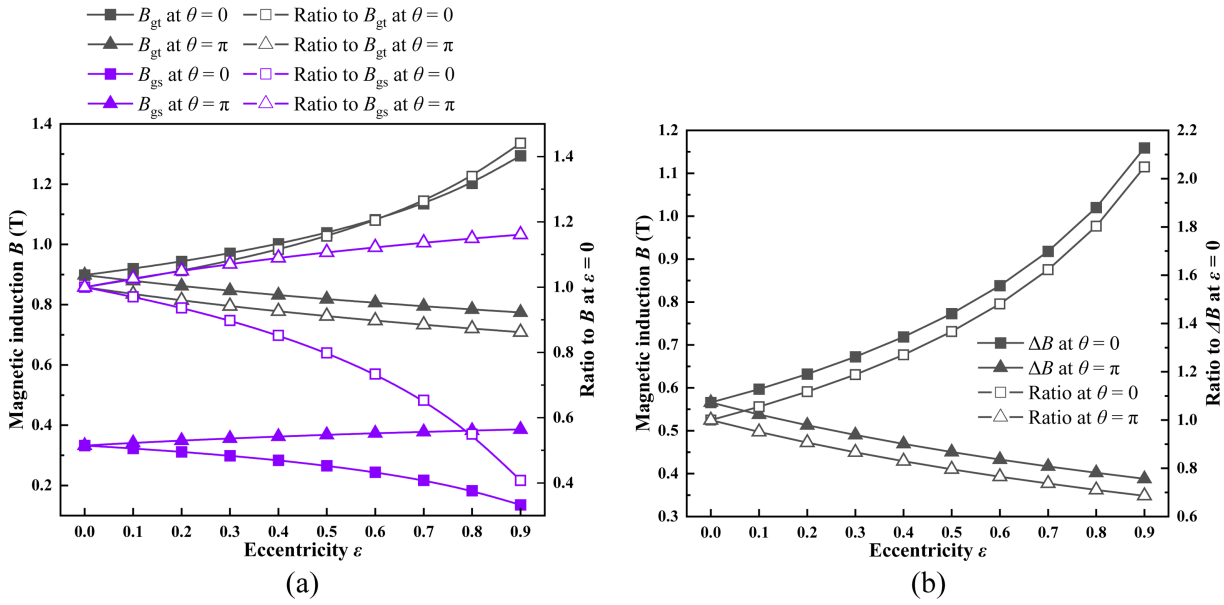

Fig. 8. (Color online) Magnetic induction vs. eccentricity: (a) B_{gt} and B_{gs}; (b) ΔB.

(2|CD|)]. When ε increases from 0 to 0.9, |CD| decreases from L_g to 0.1 times L_g at θ = 0, while λ_{gs}^{ed} rapidly increases by 1.1 times; at $\theta = \pi$, |CD| increases from L_g to 1.9 times L_g, while λ_{gs}^{ed} decreases by only 29%. According to Eq. (32), the proportion of λ_{t+gt}^{d} in λ_{pa}^{d} is proportionally larger than that of λ_{gs}^{ed}. Therefore, the trend of λ_{pa}^{d} is closer to that of λ_{t+gt}^{d}. Fig. 8 shows the B_{gt}, B_{gs} and ΔB (B_{gt}-B_{gs}) calculated by MCAM. Eq. (35) indicates a positive correlation between F_p^d and R_{pa}^d/R_{total}^d, where reducing R_{pa}^d leads to a decrease in F_p^d.

As shown in Fig. 8(a), B_{gt} increases while B_{gs} decreases at θ = 0 with ε's increase, as R_{gt}^{ed} and R_{gs}^{ed} decrease simultaneously. The reduction of F_p^d lies between the decrease rates of R_{gt}^{ed} and R_{gs}^{ed}, leading to increased B_{gt} and decreased B_{gs}, favoring B_{gt}'s increase. At $\theta = \pi$, the opposite occurs, where both R_{gt}^{ed} and R_{gs}^{ed} increase, resulting in an increase in F_p^d. However, since F_p^d's increase is smaller than that of R_{gs}^{ed} and larger than that of R_{gt}^{ed}, B_{gt} decreases while B_{gs} increases. The decrease in B_{gt} equals the increase in B_{gt} due to similar reduction rates of R_{gt}^{ed} and R_{gs}^{ed} at $\theta = \pi$.

According to Eq. (38), the pressure resistance of MFS is proportional to ΔB. As shown in Fig. 8(b), the increase in ΔB is rapidly observed at θ = 0, with the maximum value reaching twice that of no eccentricity. Meanwhile, at $\theta = \pi$, ΔB exhibits an approximately linear decrease, with the highest value nearing 40 %, in agreement with the research results of Sreedhar [28] and Zhao [29].

3.2. Calculation results of FEM

In case of eccentric MFS, a decrease in sealing gap occurs on one side and an increase on the opposite side, leading to significantly stronger magnetic induction on the side with decreased sealing gap. The shaft in Fig. 9 is offset to the right, which is consistent with Fig. 4. The dotted line indicates the axis of the pole shoe, and the magnetic induction line protrudes to the left of the dotted line, further confirming the enhancement of magnetic induction on the right side, where the sealing gap is decreased.

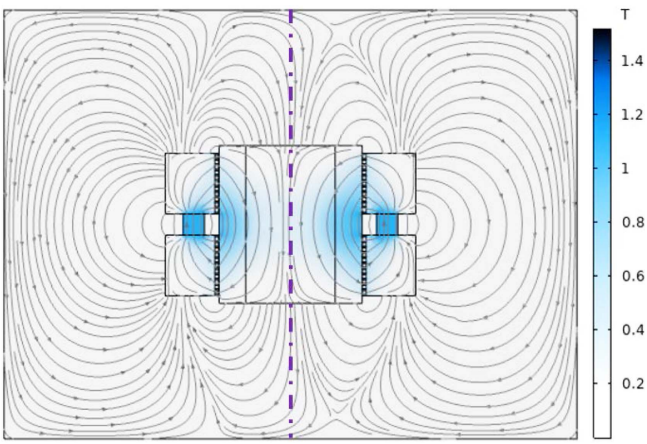

Fig. 9. (Color online) Magnetic induction and magnetic induction line when the shaft is eccentric.

Figure 10 presents B_{gt}, B_{gs}, ΔB, and the magnetic force on the shaft F_s obtained by FEM and MCAM. B_{gt} variation obtained by FEM is consistent with that obtained by MCAM. As L_g increases, B_{gt} decreases slowly with larger changes. While the results indicate that MCAM is

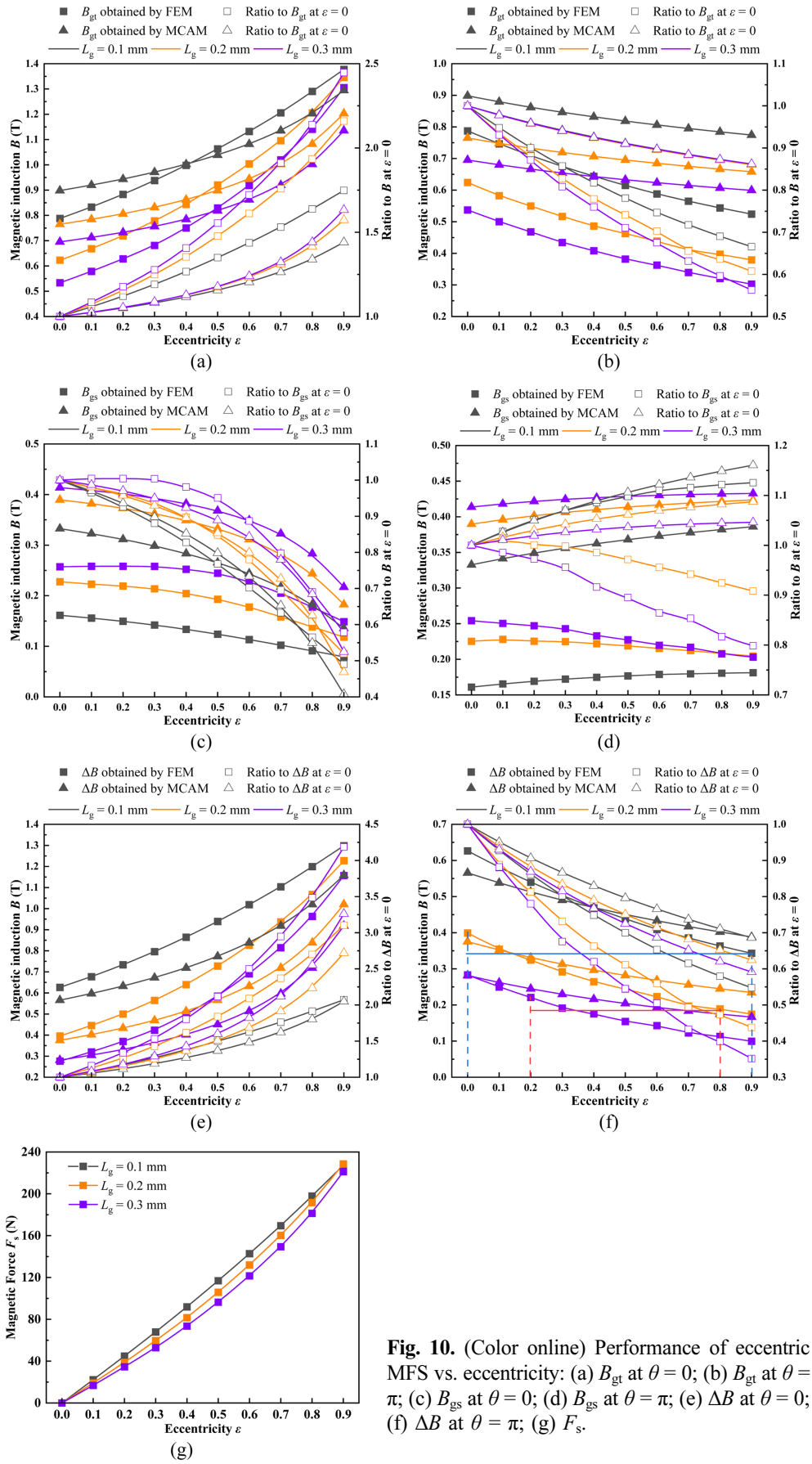

Fig. 10. (Color online) Performance of eccentric MFS vs. eccentricity: (a) B_{gt} at $\theta = 0$; (b) B_{gt} at $\theta = \pi$; (c) B_{gs} at $\theta = 0$; (d) B_{gs} at $\theta = \pi$; (e) ΔB at $\theta = 0$; (f) ΔB at $\theta = \pi$; (g) F_s.

feasible, numerical differences exist in B_{gt} obtained by FEM and MCAM at $\theta = 0$. Neglect of magnetic leakage in MCAM may be the reason. Likewise, ΔB obtained by both methods are highly consistent despite MCAM showing larger B_{gt} and B_{gs}. Comparing Figs. 10(a) and 10(b), the relative error between the results obtained by the two methods progressively decreases at $\theta = 0$, but gradually increases at $\theta = \pi$. This is because when the shaft is eccentric, the permanent magnet provides a larger magnetic motive force to the side with the smaller sealing gap than the theoretical magnetic motive force obtained by Eq. (35), while the opposite is true for the side with the larger sealing gap.

The variation of B_{gs} obtained by FEM and MCAM are shown in Figs. 10(c) and 10(d). B_{gs} obtained by MCAM is much larger than that obtained by FEM, and the relative error between them decreases at $\theta = 0$, and increases at $\theta = \pi$. This indicates that the λ_{gs} obtained by the substitution angle method is larger, and the substitution angle method is more suitable for the case of smaller L_g.

If magnetic leakage is considered, MCAM is equivalent to the 2-D axisymmetric FEM model. At any θ, the physical quantities in the range of dθ are extended to the range of 2π, which can be regarded as a 2-D axisymmetric FEM model of MFS with sealing gap of $|\mathrm{CD}|_\theta$ and no eccentricity. Therefore, the utilization of a 2-D axisymmetric FEM model to analyze the performance of eccentric MFS inevitably leads to a significant deviation in the prediction results. This is mainly due to the additional change in magnetic motive force caused by the change in reluctance. Fig. 11 clearly demonstrates the comparative outcomes obtained from the 2-D axisymmetric and 3-D FEM models, indicating an increasing relative error as with ε increases, with the maximum discrepancy being as high as 28 %.

The ΔB obtained by both methods are in good agreement in terms of value and variation, although the B_{gt} and B_{gs} obtained by the MCAM are generally larger than those obtained by the FEM, as shown in Figs. 10(e) and 10(f). The relative error between the two methods does not exceed 20 % for $\varepsilon < 0.5$. The pressure resistance of MFS is determined by the minimum pressure resistance, which is present on the larger sealing gap side (at $\theta = \pi$). The pressure resistance decreases approximately linearly as ε increases. When ε increases from 0 to 0.9, the pressure resistance decreases by up to about 65 %. The pressure resistance decreases rapidly with increasing L_g [30, 31]. For every 0.1 mm reduction in L_g, the pressure resistance can be increased by 40 % to 100 %.

As shown in Fig. 10(f), the pressure resistance of the MFS decreases slowly as ε increases. The pressure

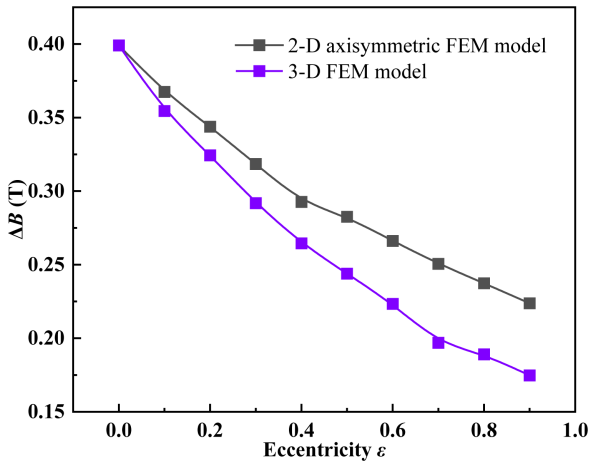

Fig. 11. (Color online) ΔB obtained from the 2-D axisymmetric FEM model and the 3-D FEM model.

resistance increases as the sealing gap decreases; however, MFSs with a large sealing gap and a minor eccentricity demonstrate better pressure resistance when $|CD|$ is similar, proven by the blue and red lines in the figure. The right point of the blue line is $L_g = 0.1$ mm, $\varepsilon = 0.9$, and $|CD|_{max} = 1.9$ mm, while its left point is $L_g = 0.2$ mm, $\varepsilon = 0$, and $|CD|_{max} = 2.0$ mm. The left point possesses a larger sealing gap, but its pressure resistance surpasses that of the right point. The right point of the red line is $L_g = 0.2$ mm, $\varepsilon = 0.9$, and $|CD|_{max} = 3.6$ mm, while its left point is $L_g = 0.3$ mm, $\varepsilon = 0.2$, and $|CD|_{max} = 3.6$ mm. MFSs with more massive sealing gaps and smaller eccentricities have better pressure resistance at the similar actual sealing gap. This indicates that when there is a certain eccentricity value, the method of increasing the sealing gap and decreasing the eccentricity can improve the pressure resistance of the MFS. However, the eccentricity of the shaft is constantly changing during actual operation. The MFS with large sealing gap has a weaker pressure resistance when the eccentricity is small. To enhance the MFS's comprehensive performance, the sealing gap must be minimized while preventing shaft-pole teeth contact and friction, and at least one redundancy in pressure resistance is necessary to avoid seal failure.

F_s is shown in Fig. 10(g), where F_s is approximately linear with ε, and has little relationship with L_g, which is in consistent with the findings of the literature [20]. In this study, with a single magnetic source, the maximum F_s is roughly 220 N. When the MFS includes several magnetic sources, F_s rapidly escalates. As F_s and ε collaboratively reinforce each other, meaning an increment in one will result in a rise in the other, the MFS design with several magnetic sources must take into account the magnetic force impact on the shaft's eccentricity.

4. Effect of Shaft Diameter on the Performance of Eccentric MFS

The focus of this study is on the MFS with a large diameter, as the radial internal clearance of the bearing typically increases with the inner diameter of the bearing. The variation of reluctance and magnetic induction with shaft diameter was calculated using the MCAM, as depicted in Fig. 12, with L_g = 0.2 mm and ε = 0.4.

Figure 12(a) and (b) show the variation of various reluctances with the shaft diameter, including R_m^d, R_{t+gt}^d, R_{gs}^{ed}, R_p^d, R_a^d and R_{pa}^d. It is important to note that the data in the figure also need to be divided by $\mu_0 d\theta$ to obtain the actual reluctance values. Each reluctance decreases as the shaft diameter increases, with the fastest change occurring in R_a^d. This is due to the proportional relationship between the shaft cross-sectional area and the square of the shaft diameter. The change trend of each other reluctance is similar. Furthermore, while R_m^d is in the same order of magnitude as R_{t+gt}^d and R_{gs}^{ed}, R_{pa}^d, as the parallel sum of the R_{t+gt}^d and R_{gs}^{ed} of multi-pole teeth, decreases as the number of pole teeth increases. In the case of 12 pole teeth and 11 tooth slots, R_{pa}^d is much smaller than R_m^d, and is in the same order of magnitude as R_p^d and R_a^d, as shown in Fig. 12(b).

The proportion of R_{pa}^d in R_{total}^d decreases as the shaft diameter increases, as shown in Fig. 12(c), although each reluctance decreases progressively, which means that F_p^d is smaller with the fixed F_c. Accordingly, B_{gt} and B_{gs} decreases with the increase of the shaft diameter. However, when the shaft diameter exceeds 150 mm, B_{gt}, B_{gs} and ΔB change at a slower rate, especially ΔB at $\theta = \pi$. At a shaft diameter of 300 mm, ΔB is 96.1 % of the ΔB at 150 mm, 92.6 % of the ΔB at 100 mm and 79.8 % of the ΔB at 40 mm. Therefore, the sealing performance of MFS with a large diameter can be estimated based on an MFS with a shaft diameter around 100 mm.

It is difficult to calculate the performance of MFS with large diameter using the FEM because the 3-D magnetic field model contains not only the pole shoe, the shaft and

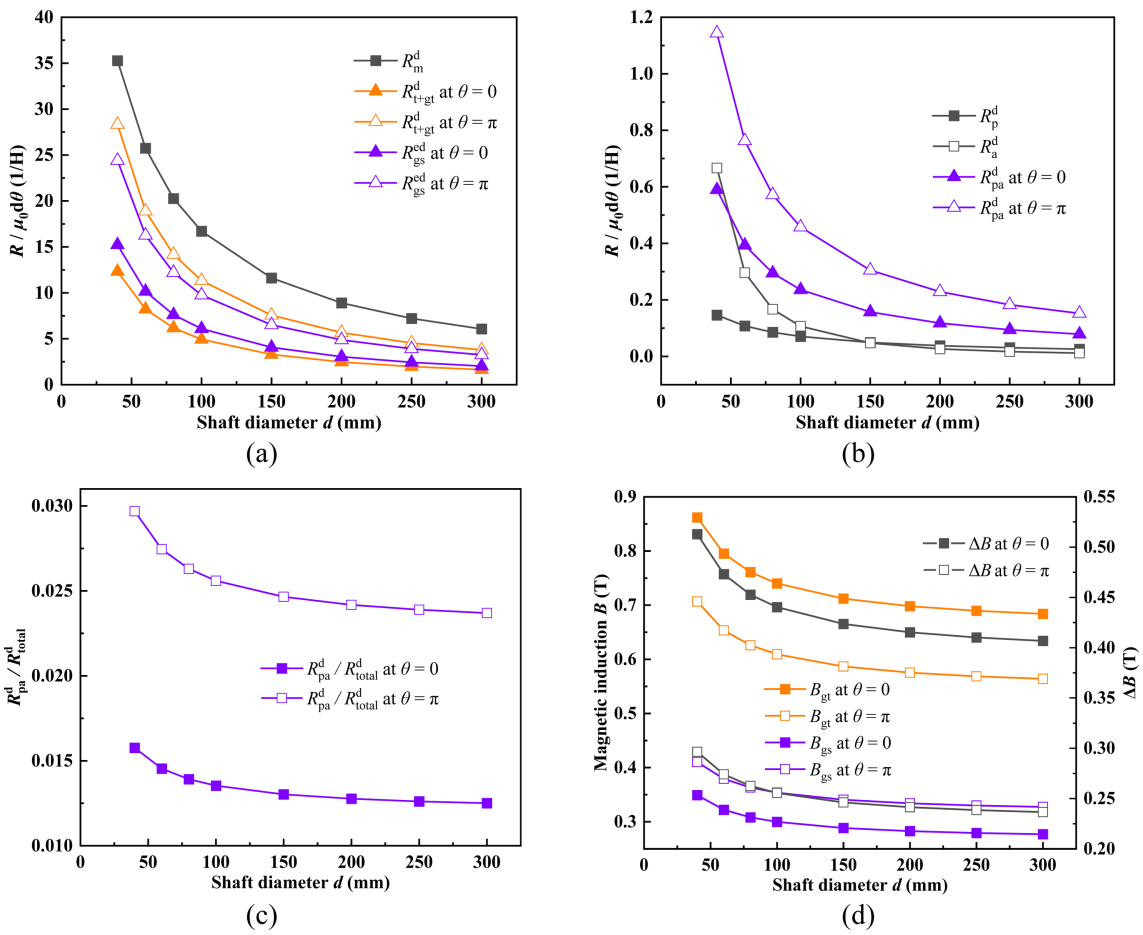

Fig. 12. (Color online) Variation of reluctance and magnetic induction with shaft diameter: (a) R_m^d, R_{t+gt}^d and R_{gs}^{ed}; (b) R_p^d, R_a^d and R_{pa}^d; (c) R_{pa}^d / R_{total}^d; (d) B_{gt}, B_{gs} and ΔB.

the permanent magnet, but also a large enough space. As the shaft diameter increases, the volume of the computational domain increases rapidly and the number of meshes divided by the same rules increases linearly, as shown in Fig. 13(a). As a result, this study utilizes FEM to calculate the sealing performance for shaft diameters

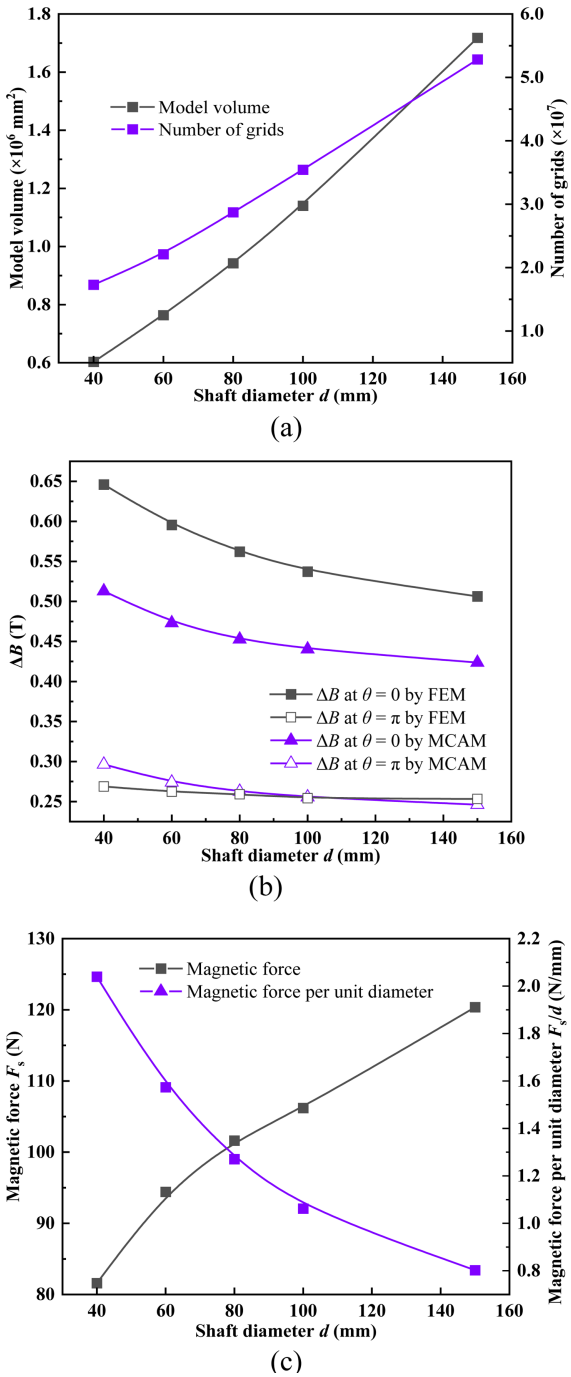

Fig. 13. (Color online) Sealing performance of eccentric MFS vs. shaft diameter: (a) model volume and number of meshes; (b) ΔB obtained by FEM and MCAM; (c) F_s.

ranging from 40 to 150 mm, with consistent evaluation conditions as MCAM.

The FEM-calculated variations of B_{gt} and B_{gs} agree with those from MCAM in Fig. 12(d), while the numerical agreement and discrepancies follow Section 3.2's conclusions and will not be discussed further. As shown in Fig. 13(b), the minimum pressure resistance of an eccentric MFS under magnetic leakage and uneven magnetic motive force distribution is noted to be almost independent of shaft diameter. An increase in shaft diameter from 40 to 150 mm results in just a 4.7 % decrease in ΔB at $\theta = \pi$, with only a 0.3 % relative error in pressure resistance between d = 150 mm and d = 100 mm. Such observations in sealing performance suggest that a more accurate sealing performance of MFS with large diameter can be obtained by calculating the model with a shaft diameter of 100 mm.

Figure 13(c) shows that increasing shaft diameter results in a nearly linear increase in F_s, especially beyond 80 mm. However, this increased magnetic force leads to greater shaft eccentricity within the radial internal clearance of the bearing, subsequently causing a decline in MFS sealing performance. For the MFS structure with single magnetic source and double pole shoe studied in this paper, the magnetic force on the large-diameter shaft can be estimated to be 0.8~1.3 times of the shaft diameter when the permanent magnet width is 6mm and thickness is 4 mm.

In summary, since the pressure resistance of MFS is determined by the weakest point, the sealing performance of the MFS with large shaft diameter can be estimated from the calculations of a model with a small shaft diameter. However, the magnetic force on the shaft can only be estimated from the shaft diameter.

5. Methods to Improve the Sealing Performance of Eccentric MFS

According to Eq. (7), the pressure resistance of the MFS is determined by the saturation magnetization strength of the magnetic fluid (M_s) and the cumulative sum of ΔB, so the magnetic fluid with high M_s can be used to improve the sealing performance [32], but this study focuses on how to increase the sum of ΔB. According to Eqs. (36) and (37), B_{gt} is related to F_p^d and $(R_t^d + R_{gt}^{ed}) \cdot A_{gt}^d$, while B_{gs} is related to F_p^d and $R_{gs}^{ed} \cdot A_{gs}^d$.

5.1. Increase of magnetic potential F_p^d

F_p^d is provided by the permanent magnets, and Eq. (35) can be rewritten as:

$$F_{\mathrm{p}}^{\mathrm{d}} = H_{\mathrm{c}} T_{\mathrm{h}} \cdot \frac{R_{\mathrm{pa}}^{\mathrm{d}}}{R_{\mathrm{m}}^{\mathrm{d}} + 2R_{\mathrm{p}}^{\mathrm{d}} + 2R_{\mathrm{pa}}^{\mathrm{d}} + R_{\mathrm{a}}^{\mathrm{d}}} = H_{\mathrm{c}} \cdot \frac{R_{\mathrm{pa}}^{\mathrm{d}}}{\dfrac{2\pi}{\mu_0 \mu_{\mathrm{r1}} A_{\mathrm{m}} \mathrm{d}\theta} + \dfrac{2R_{\mathrm{p}}^{\mathrm{d}} + 2R_{\mathrm{pa}}^{\mathrm{d}} + R_{\mathrm{a}}^{\mathrm{d}}}{T_{\mathrm{h}}}} \tag{39}$$

The above equation shows that the permanent magnet parameters related to $F_{\mathrm{p}}^{\mathrm{d}}$ include H_{c}, A_{m} and T_{h}. Where increasing H_{c} directly increases $F_{\mathrm{p}}^{\mathrm{d}}$, increasing A_{m} is equivalent to reducing $R_{\mathrm{m}}^{\mathrm{d}}$, while increasing T_{h} is equivalent to reducing the percentage of $R_{\mathrm{m}}^{\mathrm{d}}$ in $R_{\mathrm{total}}^{\mathrm{d}}$. Both A_{m} and T_{h} increase the proportion of $R_{\mathrm{pa}}^{\mathrm{d}}$ by changing $R_{\mathrm{m}}^{\mathrm{d}}$, so as to increase $F_{\mathrm{p}}^{\mathrm{d1}}$.

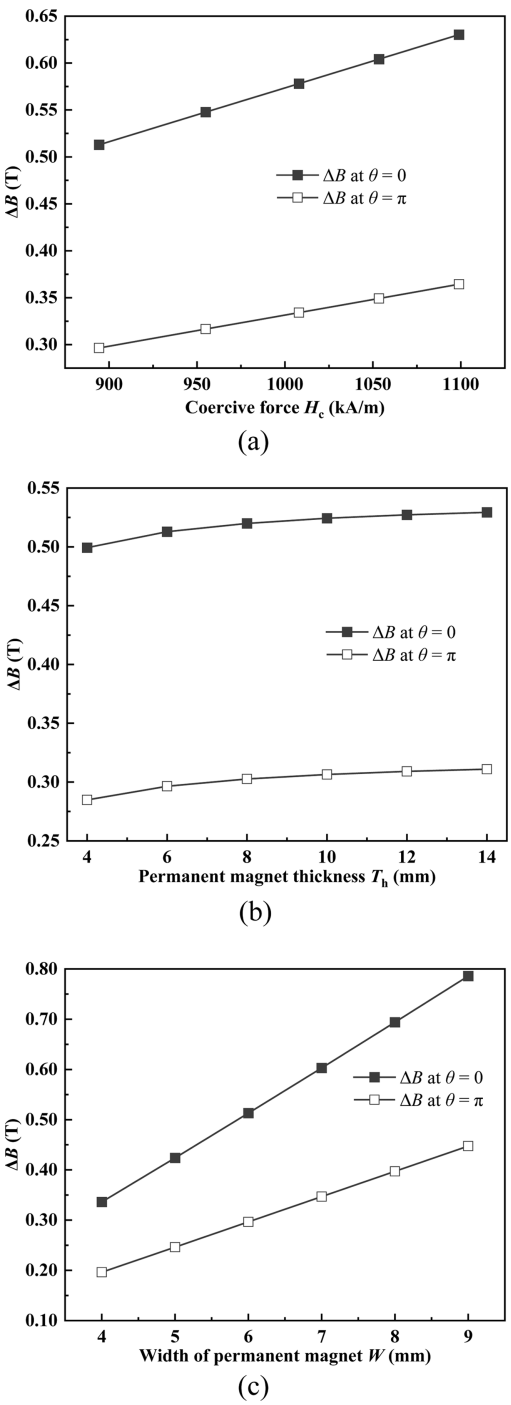

Fig. 14. Relationship between ΔB and permanent magnet parameters: (a) H_{c}; (b) T_{h}; (c) W.

Figure 14(a) displays a linear relationship between ΔB and H_{c}, with an increase in H_{c} potentially leading to a 23 % augmentation in pressure resistance. In Fig. 14(b), T_{h} has a remarkable effect on ΔB [33], particularly on a thin permanent magnet. When T_{h} increases from 4 mm to 8 mm, ΔB rises by 7.6 %. However, as the permanent magnet's thickness increases, the impact of T_{h} weakens. For example, when T_{h} increases from 10 mm to 14 mm, ΔB only increases by 1.5 %.

Figure 14(c) shows the effect of the permanent magnet width (W) on ΔB. Since W is a widely used parameter, it replaces A_{m}. Increasing W can significantly reduce $R_{\mathrm{m}}^{\mathrm{d}}$ and increase the percentage of $R_{\mathrm{pa}}^{\mathrm{d}}$. By increasing W from 4 mm to 9 mm, ΔB can increase by as much as 128 %. Since both B_{gt} and B_{gs} obtained by MCAM are average values and does not consider the impact of local magnetic saturation on the magnetic field, an excessive W could elevate calculation errors. Even so, increasing W considerably enhances the sealing performance of an eccentric MFS.

5.2. Increasing the magnetic induction difference

According to Eqs. (37) and (38), ΔB can be rewritten as

$$\Delta B = B_{\mathrm{gt}} - B_{\mathrm{gs}} = F_{\mathrm{p}}^{\mathrm{d}} \left(\frac{1}{R_{\mathrm{t+gt}}^{\mathrm{d}} A_{\mathrm{gt}}^{\mathrm{d}}} - \frac{1}{R_{\mathrm{gs}}^{\mathrm{ed}} A_{\mathrm{gs}}^{\mathrm{d}}} \right) = F_{\mathrm{c}} \frac{R_{\mathrm{pa}}^{\mathrm{d}}}{R_{\mathrm{total}}^{\mathrm{d}}} \left[\frac{\mu_0 \mu_{\mathrm{r2}} R_2}{R_1 L_{\mathrm{h}} + \mu_{\mathrm{r2}} R_2 |CD|} - \frac{2\mu_0 \ln\left(1 + \dfrac{\beta L_{\mathrm{s}}}{2|CD|}\right)}{\beta L_{\mathrm{s}}} \right] \tag{40}$$

Since $R_{\mathrm{gs}}^{\mathrm{ed}}$ is calculated by the substitution angle method, the height of pole tooth (L_{h}) solely impacting $R_{\mathrm{t}}^{\mathrm{d}}$ rather than $R_{\mathrm{gs}}^{\mathrm{ed}}$. According to Eq. (40), $(R_{\mathrm{t}}^{\mathrm{d}} + R_{\mathrm{gt}}^{\mathrm{ed}}) \cdot A_{\mathrm{gt}}^{\mathrm{d}}$ is related to R_1, L_{h} and $|CD|$, while $R_{\mathrm{gs}}^{\mathrm{ed}} \cdot A_{\mathrm{gs}}^{\mathrm{d}}$ is related to the width of tooth slot (L_{s}) and $|CD|$. Fig. 15 shows the variation of the term in parentheses with L_{h} and L_{s}, and the values in the figure are the ratios to the result of L_{h} = 1 mm and L_{s} = 1 mm. The research reveals that changing merely L_{h} has little impact on sealing performance as shown in Fig. 15(a). This finding differs from that of earlier research primarily because $R_{\mathrm{gs}}^{\mathrm{ed}}$ is calculated using the substitution angle method without taking L_{h} into account, and L_{h} has no impact on $R_{\mathrm{gs}}^{\mathrm{ed}}$. An appropriate increase in L_{s} can

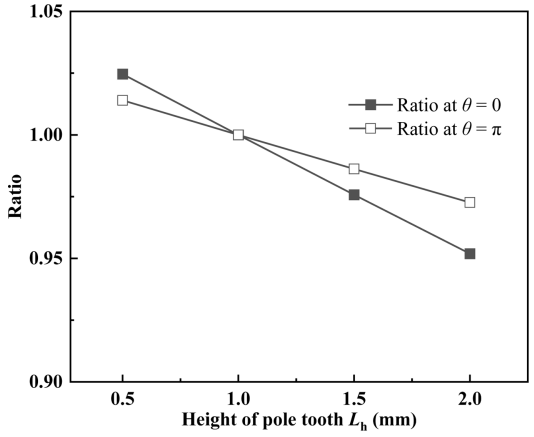

(a)

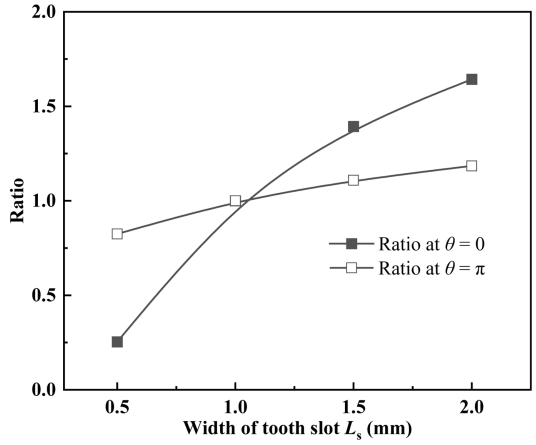

(b)

Fig. 15. Variation of the terms in parentheses of Eq. (40) with L_h and L_s: (a) L_h; (b) L_s.

enhance sealing effectiveness by 18 % when it goes from 0.5 to 1 mm. An excessive increase in L_s, however, can lead to an elongated seal and a decreased number of pole teeth, both of which undermine sealing efficiency.

To amplify ΔB, the primary strategy is to increase R_{pa}^{d}, a variable related to R_{t+gt}^{d}, R_{gs}^{ed} and the number of pole teeth (n_p) as per Eq. (31). However, R_{t+gt}^{d} depends on the thickness of the pole teeth (L_t), while R_{gs}^{ed} is associated with L_s. In turn, the variables of n_p, L_t, and L_s are also relevant to R_a^d and R_p^d, making it challenging to examine the impact of a single variable on MFS sealing performance. Fig. 16(a) and (b) indicate that decreasing L_t [34, 35] and increasing L_s [33, 35] can increase ΔB. The recommended optimal values for L_t and L_s are 0.3-0.5 mm and 0.7-1.3 mm, respectively, considering the sealing performance and sealing length. Meanwhile, Fig. 16(c) suggests that increasing n_p results in a decline in R_{pa}^{d} and the proportion of R_{pa}^{d} in R_{total}^{d}, yet n_p compensates for the

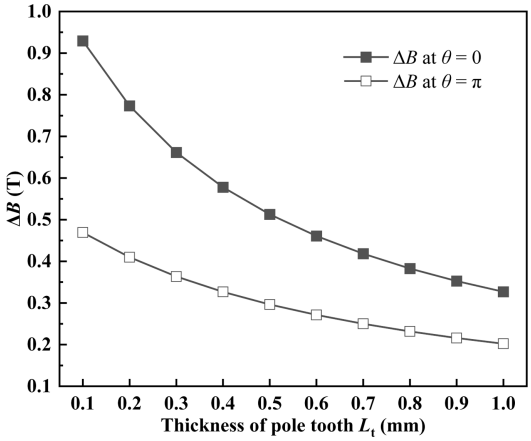

(a)

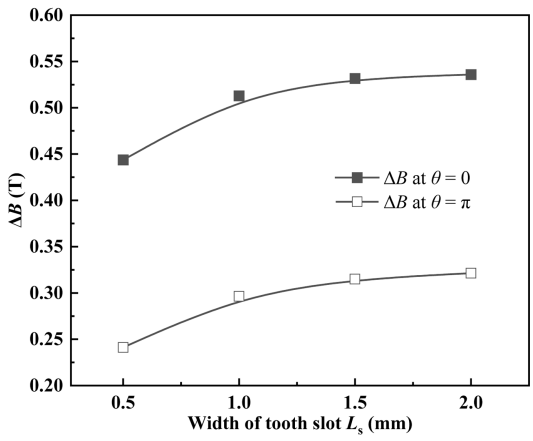

(b)

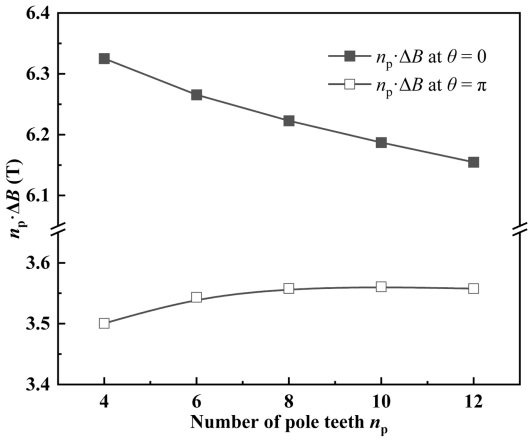

(c)

Fig. 16. Relationship between sealing performance of MFS and pole tooth parameters: (a) L_t; (b) L_s; (c) n_p.

reduced sealing pressure per pole tooth, with $n_p \cdot R_{pa}^{d}$ initially elevating [36, 37], peaking at n_p = 10, and then decreasing.

6. Conclusion

(1) The most crucial factors influencing the sealing performance of eccentric MFS are the sealing gap and eccentricity. The major causes of the decrease in sealing performance when the shaft is eccentric are the uneven magnetic field distribution in the sealing gap and the rise in reluctance on the side with the larger sealing gap. The pressure resistance decreases approximately linearly as ε increases. When ε increases from 0 to 0.9, the pressure resistance decreases by up to about 65 %. The sealing gap should be minimized while preventing contact and friction between the shaft and the pole teeth, and there should be a redundancy of at least one times the pressure resistance to avoid seal failure. The eccentricity is the most important factor that affects the magnetic force on the shaft.

(2) As the shaft diameter increases, the magnetic field in the sealing gap gradually decreases, but the magnetic induction of the side with the larger sealing gap changes very little, and the pressure resistance of MFS decreases by no more than 5 %, so a model with a shaft diameter of 100 mm can be used to accurately predict the sealing performance of MFS with larger shaft diameters. The magnetic force on the shaft varies approximately linearly with the shaft diameter. For the MFS structure with single magnetic source and double pole shoe studied in this paper, the magnetic force on the large-diameter shaft can be estimated to be 0.8~1.3 times of the shaft diameter when the permanent magnet width is 6 mm and thickness is 4 mm.

(3) The use of permanent magnets with a higher coercive force and an expansion of their magnetic flux areas can significantly enhance the sealing performance of eccentric MFS. For thin permanent magnets, increasing their thickness has limited impact on MFS performance. In order to improve MFS performance, a pole-tooth thickness of 0.3-0.5 mm, tooth slot width of 0.7-1.3 mm, and 10 pole teeth are recommended.

Acknowledgement

This works was supported by “the National Key R&D Program of China” (Grant No. 2020YFB2006900).

References

[1] X. Z. He, Y. B. Miao L. Wang, and D. C. Li, Chinese Journal of Vacuum Science and Technology **39**, 361 (2019).
[2] S. Odenbach, J. Phys-Condens. Mat. **16**, 1135 (2004).
[3] D. K. Devendiran and V. A. Amirtham, Renew. Sust. Energ. Rev. **60**, 21 (2016).
[4] Z. G. Li, J. R. Zhang, and D. Y. Li, Adv. Mech. Eng. **10**, 1687814018772369 (2018).
[5] Y. Chen and D. C. Li, Acta Armamentarii **32**, 1428 (2011).
[6] F. X. Hao and A. L. Mu, Journal of Xi'an University of Technology **38**, 27 (2022).
[7] F. F. Xing and D. C. Li, Chinese Journal of Vacuum Science and Technology **31**, 362 (2011).
[8] F. Y. Yang, S. Wang, L. Lou, Q. L. Wang, and J. H. Chen, Chinese Hydraulics & Pneumatics **03**, 63 (2009).
[9] Y. Q. Cai, D. C. Li, and D. Y. Ren, Chinese Journal of Vacuum Science and Technology **35**, 897 (2015).
[10] Z. Y. Yu and W. Zhang, Lubrication Engineering **34**, 31 (2009).
[11] X. Z. He, L. Wang, J. Yu, and D. C. Li, Int. J. Appl. Electrom. **60**, 21 (2019).
[12] Y. H. Cheng, Z. Z. Wang, and D. C. Li, J. Magn. **24**, 506 (2019).
[13] X. L. Yang, Z. L. Zhang, and D. C. Li, Sci. China. Technol. Sc. **56**, 2865 (2013).
[14] D. C. Li and D. Hao, Chinese Journal of Vacuum Science and Technology **38**, 564 (2018).
[15] M. Szczech, J. Magn. **24**, 32 (2019).
[16] X. R. Li, Z. G. Li, B. S. Zhu, J. Chen, W. X. Li, and J. Y. Yuan, J. Magn. Magn. Mater. **540**, 168472 (2021).
[17] F. F. Xing and J. Ji, Lubrication Engineering **44**, 87 (2019).
[18] X. R. Li, Z. G. Li, and Z. Q. Yan, J. Chen, Journal of Magnetic Materials and Devices **53**, 53 (2022).
[19] D. C. Li, X. Z. He, and Z. Zhang, Magnetohydrodynamics **44**, 75 (2008).
[20] S. W. Zhang and Y. Q. Li, Lubrication Engineering **01**, 55 (1995).
[21] S. W. Zhang, Y. Q. Li, and N. H. Yang, Chinese Journal of Vacuum Science and Technology **06**, 24 (1986).
[22] W. M. Yang, D. C. Li, Y. Q. Cai, Y. Huang, and Q. Li, Lubrication Engineering **34**, 48 (2009).
[23] Y. C. Zhang, J. G. Wang, and S. X. Yuan, Lubrication Engineering **01**, 51 (2004).
[24] D. C. Li, Theory and application of magnetic fluid seal, Science Press, Beijing (2010) pp. 69-73.
[25] J. A. Stratton, Electromagnetic theory, IEEE Press, New Jersey (2007) pp. 153-156.
[26] X. L. Yang, Y. Liu, Y. Guan, and G. J. Xie, Vacuum **207**, 111670 (2023).
[27] Y. Liu, J. W. Yang, D. C. Li, and Y. J. Zhang, Journal of Mechanical & Electrical Engineering **38**, 1424 (2021).
[28] B. K. Sreedhar, R. N. Kumar, P. Sharma, S. Ruhela, J. Philip, S.I. Sundarraj, N. Chakraborty, M. Mohana, V. Sharma, G. Padmakumar, B. K. Nashine, and K. K. Rajan, Nucl. Eng. Des. **265**, 1166 (2013).
[29] M. Zhao, J. B. Zou, and J. H. Hu, J. Magn. Magn. Mater. **303**, e428 (2021).

[30] X. R. Li, Z. G. Li, B. S. Zhu, J. Cheng, W. X. Li, and J. Y. Yuan, J. Magn. Magn. Mater. **540**, 168472 (2021).
[31] Y. J. Zhang, Y. B. Chen, D. C. Li, Z. M. Yang, and Y. L. Yang, IEEE T. Magn. **55**, 4600308 (2019).
[32] S. Parmar, V. Ramani, R. V. Upadhyay, and K. Parekh, Vacuum. **172**, 109087 (2020).
[33] F. Chen, X. L. Yang, S. H. Gao and Y. H. Chen, Int. J. Appl. Electrom. **55**, 535 (2017).
[34] H. T. Zhang and D. C. Li, J. Magn. **22**, 133 (2017).
[35] J. B. Zou and Y. P. Lu, IEEE T. Magn. **28**, 3361 (1992).
[36] X. L. Yang, Y. Guan, Y. Li, and D. C. Li, Tribol. T. **64**, 1046 (2021).
[37] S. J. Liu, D. C. Li, X. Z. H, and Z. L. Zhang, Front. Mater. **9**, 932697 (2022).